Supporting Material

This is the supporting material for the manuscript:

Keijser, J., Hertäg, L. & Sprekeler, H., 2023. Transcriptomic correlates of state modulation in GABAergic interneurons: A cross-species analysis. *bioRxiv*, pp.2023-12.

Replication of Bugeon et al.

We validated our analysis pipeline by replicating the relevant results from Bugeon et al. [9] on their data. These data consist of in vivo neural activity and in situ gene expression of neurons from layers 1-3 of mouse primary visual cortex (*Mus musculus* VISp). Expression data was limited to a panel of 72 genes previously selected to identify interneuron subtypes [45]. The data also contain behavioural variables (e.g., running speed) that assign each time point to a "behavioural state". Bugeon et al. distinguished three possible states: running (distinguished by a positive running speed), stationary desynchronized (zero running speed and little neural oscillations), and stationary synchronised (zero running speed and prominent neural oscillations). A neuron's state modulation was defined as the normalised difference between its average activity during the most and least active state:

$$\frac{\text{running activity} - \text{synchronized activity}}{\text{running activity} + \text{synchronized activity}} \tag{4}$$

Neurons that are more active during running compared to baseline will therefore have a positive state modulation. In contrast, neurons that are less active during running will have a negative state modulation.

We selected high-quality cells following the criteria from Bugeon et al. ([9], see Materials and Methods), resulting in the same number of 1,065 inhibitory interneurons reported in their work. These interneurons are hierarchically distributed across 5 subclasses and 35 subtypes. State modulation could be computed for 872 neurons recorded during both running and synchronized states. As previously reported, visualising the neural activity during these states suggested differential state modulation between both cell classes and subtypes (Fig. S1a). We then computed each neuron's state modulation based on its time-averaged activity (Equation (4)). Consistent with ref. [9], state modulation was negative for Pvalb (Pearson correlation -0.13), small and positive for Sst and Lamp5 (both 0.02), and strongly positive for Vip and Sncg interneurons (0.13 and 0.21, respectively) (Fig. S1b).

Next, we aimed to replicate the correlation between the first transcriptomic principal component (tPC1) and the state modulation. To compute tPC1, we first normalised and log-transformed the cell-by-gene expression matrix to correct for differences in sequencing depth and to stabilise the gene-count variances. We then applied principal component analysis to the transformed matrix. State modulation could indeed be predicted from tPC1 projections, both for subtypes (Fig. S1c, leave-one-out $R^2 = 0.19$) and for individual neurons ($R^2 = 0.17$). The predictive power of tPC1 is to some extent driven by between-subclass differences in gene expression [37] since it is relatively modest within individual subclasses (Fig. S2). Additional tPCs contained less information

regarding state modulation: the second-best tPC (tPC29) achieved an R^2 of 0.10 and explained only 0.9% of the variance, and tPC2 did not predict state modulation at all ($R^2 = -0.01$, Fig. S3). Together, the first 30 tPCs improved upon tPC1 ($R^2 = 0.60$, 76.2% of total variance).

Finally, we verified the correlation between state modulation and cholinergic receptor expression that might reflect a mechanistic link between state modulation and transcriptome [9]. Since cholinergic receptor expression was not measured for the in vivo recorded neurons (the 72 gene panel did not include these receptors), its relationship with state modulation can only be tested using external expression values. Following ref. [9], we obtained these values from the publicly available data of Tasic et al. [6]. We preprocessed the raw count data like the Bugeon et al. expression matrix and selected the 35 upper-layer subtypes present in the in vivo data. We then computed the average receptor expression of each subtype and compared this with its average state modulation. Linear regression showed that the expression of 5 out of 15 cholinergic receptors (or receptor subunits) could predict state modulation (Figs. S1d, S11). These consist of the 4 receptors shown by Bugeon et al. (Chrm3,4 and Chrna4,5, their Fig. 6b) and an additional nicotinic receptor (Chrna3).

We found one qualitative difference with previous results (Fig. 5c in ref. [9]), namely a clustering of tPC1 scores into two groups corresponding to developmental origin [38]. This was caused by the log transformation used here but not in the original analyses (Fig. S3). The log transformation is a widely used preprocessing step in the analysis of count data [90, 91]. However, other transformations are also possible (see, e.g., [92, 93]). Here, it had only a minor effect on the quantitative relationship between tPC1 and state modulation (Fig. S3).

Network analysis

The cholinergic receptor densities in our simulations were chosen consistently with the transcriptomic and activity data, but other choices are also possible, of course. We therefore investigated the effect of varying receptor densities using mathematical analyses. In particular, we asked for which receptor densities the cholinergic effect might be different from that in the mouse. For example: does the lack of inhibitory receptors in human Pvalb cells imply that these cells are not inhibited during cholinergic modulation? And does the expression of inhibitory receptors by turtle Sst cells imply that these cells are actually inhibited?

In our simulations, all neurons receive net-positive inputs. Under these conditions, the network model contains only one nonlinearity: the rectification of dendritic activity that reaches the soma. The rectification is piecewise linear: if the dendrites are excited, the dendrites influence the soma ($w_{ed} = 1$); if the dendrites are inhibited, the dendrite remains inactive and decouple from the soma ($w_{ed} = 0$). The network dynamics are, therefore, governed by one of two connectivity matrices that only differ in the entry w_{ed}. Otherwise, the dynamics are linear:

$$\dot{\mathbf{r}} = -\mathbf{r} + W(w_{ed})\mathbf{r} + \mathbf{I}_0 + \mathbf{m}. \tag{5}$$

Here, $\mathbf{m}$ is the vector modelling cholinergic modulation, and $\mathbf{I}_0$ is the external input. For a given somato-

dendritic coupling w_{ed} and cholinergic modulation $\mathbf{m}$, the steady state rates are found by solving $\dot{\mathbf{r}} = 0$:

$$\mathbf{r}(w_{ed}, \mathbf{m}) = [I - W(w_{ed})]^{-1}[\mathbf{I}_0 + \mathbf{m}] = A(w_{ed})[\mathbf{I}_0 + \mathbf{m}], \tag{6}$$

where we defined $A(w_{ed}) = [I - W(w_{ed})]^{-1}$ as the matrix that maps inputs to steady-state rates:

$$A(w_{ed}) = \begin{pmatrix} 1 - w_{ee} & w_{ed} & -w_{ep} & 0 & 0 \\ w_{de} & 1 & 0 & -w_{ds} & 0 \\ w_{pe} & 0 & 1 + w_{pp} & -w_{ps} & 0 \\ w_{se} & 0 & 0 & 1 & -w_{sv} \\ w_{ve} & 0 & 0 & -w_{vs} & 1 \end{pmatrix}^{-1} \quad w_{ab} \geq 0 \ \ \forall a, b. \tag{7}$$

Below, we will compute the relevant entries of $A(w_{ed})$ up to its determinant, which is positive and therefore does not affect the entries' signs.

We use equation (6) to compute the modulatory effect on the network activity as the difference between the rates with and without modulation. We will consider the cases in which cholinergic modulation activates the dendrite that was silent without modulation (off→on) or inactivates the dendrite that was activated without ACh (on→off). The other two cases (on→on, off→on) can be derived analogously.

First, consider the case that modulation switches the dendrites off, as for the mouse and human circuits. The resulting change in network activity equals:

$$\Delta \mathbf{r} = \mathbf{r}(0, \mathbf{m}) - \mathbf{r}(1, \mathbf{0}) \tag{8}$$

$$= A(0)[\mathbf{I}_0 + \mathbf{m}] - A(1)[\mathbf{I}_0 + \mathbf{0}] \tag{9}$$

$$= A(0)\mathbf{m} + [A(0) - A(1)]\mathbf{I}_0. \tag{10}$$

In case that modulation switches the dendrites on, as for the turtle circuit, the resulting change in network activity equals:

$$\Delta \mathbf{r} = A(1)\mathbf{m} + [A(1) - A(0)]\mathbf{I}_0. \tag{11}$$

The first term in these equations is a linear combination of the receptor densities $\mathbf{m} = (m_e, m_d, m_p, m_s, m_v)$, describing how the cholinergic modulation of individual populations propagates through the network. In our model, pyramidal cells do not express cholinergic receptors ($m_e = m_d = 0$), such that the cholinergic effect is a linear combination of only the interneuron receptor densities. The second term in Eq. (11) is independent of the precise modulation and describes how the background input $\mathbf{I}_0$ propagates through the network with and without activated dendrites. Since this term is small, we ignore it in the following derivations, but it is shown in Fig. 5.

31

First, consider the cholinergic effect on Pvalb cells, which equals:

$$\Delta r_p = A_{pp}m_p + A_{ps}m_s + A_{pv}m_v. \tag{12}$$

Substituting the entries of $A(0)$ gives:

$$\Delta r_p = A_{pp}m_p - A_{ps}(w_{sv} \cdot m_v - m_s) \tag{13}$$

$$= (1 - w_{ee}) \cdot (1 - w_{sv} \cdot w_{vs}) \cdot m_p+ \tag{14}$$

$$w_{sv} \cdot (1 - w_{ee})(w_{ps} \cdot m_v - m_s). \tag{15}$$

An analogous equation describes Δr_s (see below). The lines in Figure 5 show $\Delta r_p = 0$ and $\Delta r_s = 0$ as a function of the Pvalb and Sst receptor densities m_p and m_s, for a fixed Vip density m_v. These boundaries delineate domains of positive and negative modulation of Pvalb and Sst interneurons.

So does the absence of inhibitory ACh receptors in human Pvalb cells (Fig. 4; $m_p = 0$) imply that these cells will not be inhibited? Equation Eq. (13) shows that these cells will still be inhibited indirectly under the condition that:

$$\Delta r_p = w_{sv} \cdot (1 - w_{ee})(w_{ps} \cdot m_v - m_s) < 0. \tag{16}$$

The coefficient $w_{sv} \cdot (1 - w_{ee})$ is positive, assuming the recurrent connectivity is not very strong ($w_{ee} \leq 1$). Inhibition of Pvalb cells is then equivalent to

$$\Delta r_p < 0 \iff w_{ps} \cdot m_v - m_s < 0. \tag{17}$$

According to the expression data, Sst and Vip cells are positively modulated ($m_s, m_v > 0$). Therefore, Pvalb cells will be inhibited by ACh as long as the inhibition from Ssts is stronger than the disinhibition from Vips. Under these conditions, the limited Chrm4 expression by human Pvalb cells is compatible with their inhibition.

Let us next consider the differential expression of inhibitory ACh receptors in Sst interneurons in turtles versus mammals. Intuitively, this is expected to cause a cholinergic suppression of Sst cells in the turtle, in contrast to the mouse. In the model, the cholinergic effect on Sst cells equals:

$$\Delta r_s = A_{sp}m_p + A_{ss}m_s + A_{sv}m_v. \tag{18}$$

Subsituting the entries from $A(1)$ gives:

$$\Delta r_s = A_{sp}m_p + A_{ss}(m_s - w_{sv} \cdot m_v) \tag{19}$$

$$= w_{ep} \cdot (w_{sv} \cdot w_{ve} - w_{se}) \cdot m_p + \tag{20}$$

$$[(1 - w_{ee} - w_{de})(1 + w_{pp}) + w_{ep} \cdot w_{pe}](m_s - w_{sv}m_s). \tag{21}$$

For the turtle circuit, $m_p \leq 0$, since Pvalb cells (weakly) express inhibitory ACh receptors. The first term will therefore be negative if $w_{sv} \cdot w_{ve} - w_{se} > 0$. Further, $m_s < 0$ and $m_v > 0$, such that $m_s - w_{sv}m_v < 0$. The contribution of the second term will therefore be negative if:

$$(1 - w_{ee} - w_{de})(1 + w_{pp}) + w_{ep} \cdot w_{pe} > 0.$$

This will be the case unless recurrent excitation is very strong or the feedback loop between PCs and Pvalb cells is very weak. In summary, the expression of inhibitory ACh receptors by turtle Sst cells will indeed lead to their cholinergic inhibition, provided that the excitation onto Sst cells and the recurrent excitation are not too strong.

Software

An Anaconda [97] environment with the appropriate software will be provided along with the code (Table 5).

Software	version
AnnData [98]	0.8.0
Matplotlib [99]	3.6.2
Numpy [100]	1.23.5
Pandas [101]	1.5.2
Python [102]	3.10.10
R [103]	4.3.0
Scanpy [104]	1.9.1
Scikit-learn [105]	1.2.1
Scipy [106]	1.9.3
Seaborn [107]	0.12.2
Seurat [108]	4.0
Snakemake [89]	7.8.2
Statsmodels [109]	0.13.5

Table 5: Software versions.
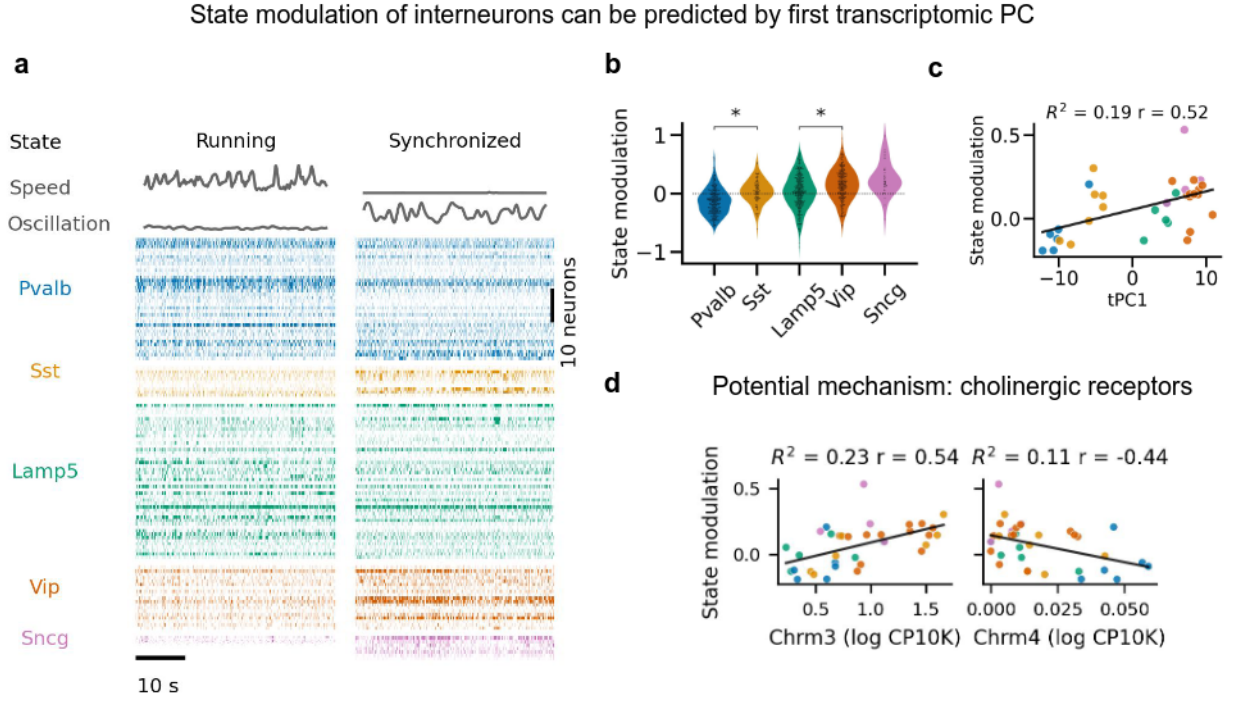
Supplementary figures

Fig. S1: Replication of previous findings from Bugeon et al. [9] (a) Neural activity systematically varies with behavioural state (measured by running speed and neural oscillations, see Materials and Methods) both between and within interneuron classes of mouse primary visual cortex (VISp) L1-3. **(b)** State modulation across all sessions for $n = 872$ interneurons. Stars indicate statistically significant differences between subclasses ($p < 0.05$, Mann-Whitney U test). **(c)** The first transcriptomic principal component (tPC1) of the cell-by-gene matrix predicts state modulation of subtypes ($n = 35$); Fig. S2a shows the relationship for individual cells. R^2, leave-one-out fraction of variance explained; r, Pearson correlation. Note the two clusters along tPC1, consisting of MGE-derived (Pvalb & Sst) and CGE-derived (Lamp5, Vip, Sncg) interneurons. **(d)** Cholinergic receptors potentially link a neuron's transcriptome and state modulation. For example, interneurons that overexpress the excitatory receptor Chrm3 are positively state-modulated ($r = 0.54$; $p = 0.0008$), those that overexpress the inhibitory cholinergic receptor Chrm4 are negatively state-modulated ($r = -0.44$, $p = 0.0075$). CP10K, counts per 10 thousand. Data and findings from Bugeon et al. [9]. Cholinergic receptor expression in (d) from Tasic et al. [6].
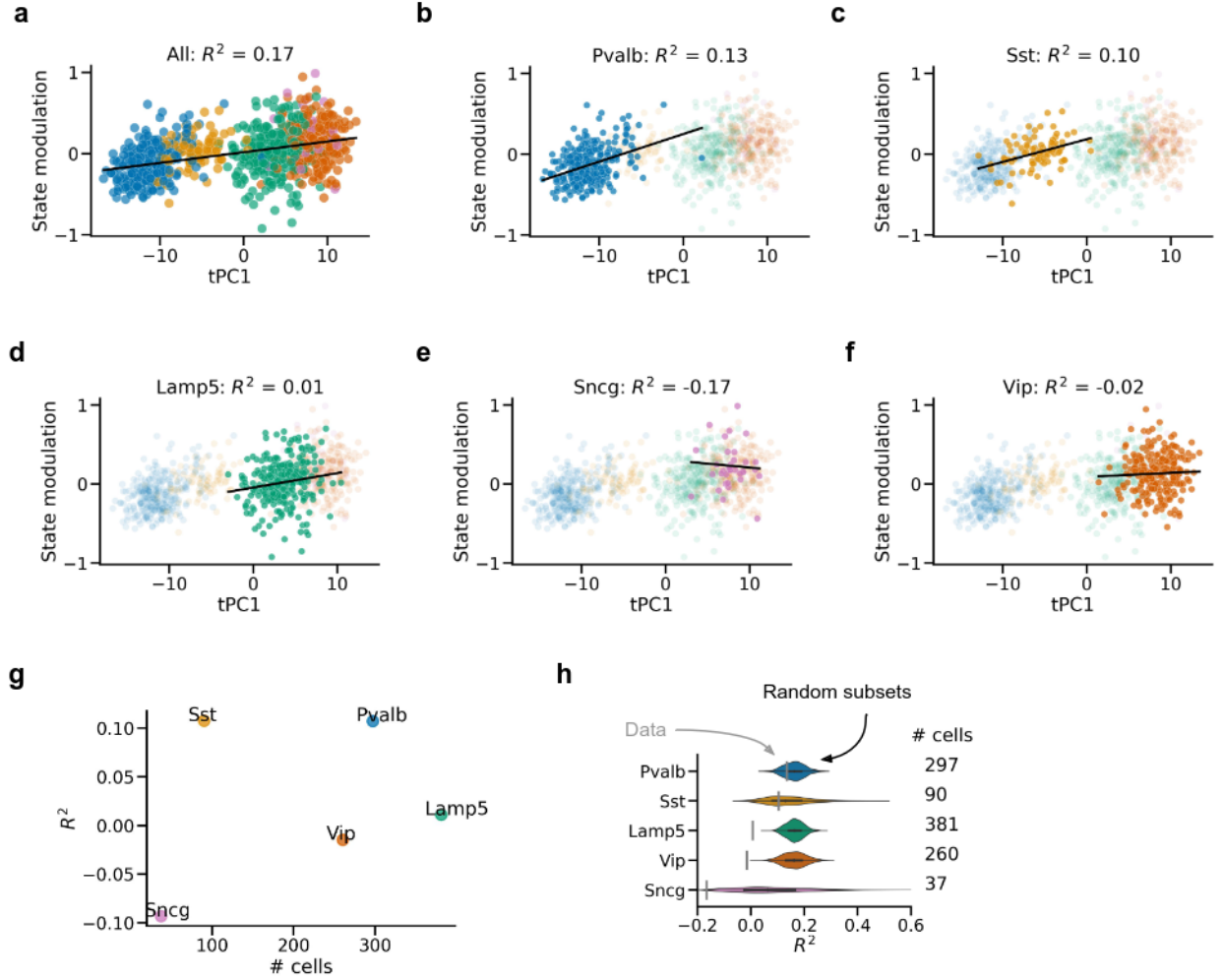
Fig. S2: Predicting state modulation from tPC1. Regression based on all cells (**a**) or cells from a single subclass (**b-f**). Predictive performance is worse for individual classes and only better than chance for Pvalb and Sst cells. The correlation between tPC1 and state modulation is therefore partially driven by between-subclass differences. However, tPC1 is still predictive of state modulation across all cells while controlling for subclass ($p = 0.003$, linear mixed model with subclass as random effect). R^2: leave-one-cell-out fraction of variance explained; $R^2 < 0$ indicates a worse fit compared to predicting the same state modulation for each cell independent of tPC1 score. (**g,h**) Poor performance for certain subclasses is not due to a smaller sample size. (**g**) Sample size is not correlated with worse performance. (**h**) Size-matched subsets of all cells outperform below-chance subclasses, except for Sst cells. Grey bars: R^2 values for each subclass. Violin plots: distribution of R^2 values for 1000 random subsets of all cells with sample size matched to the subclass. Data from Bugeon et al. [9].
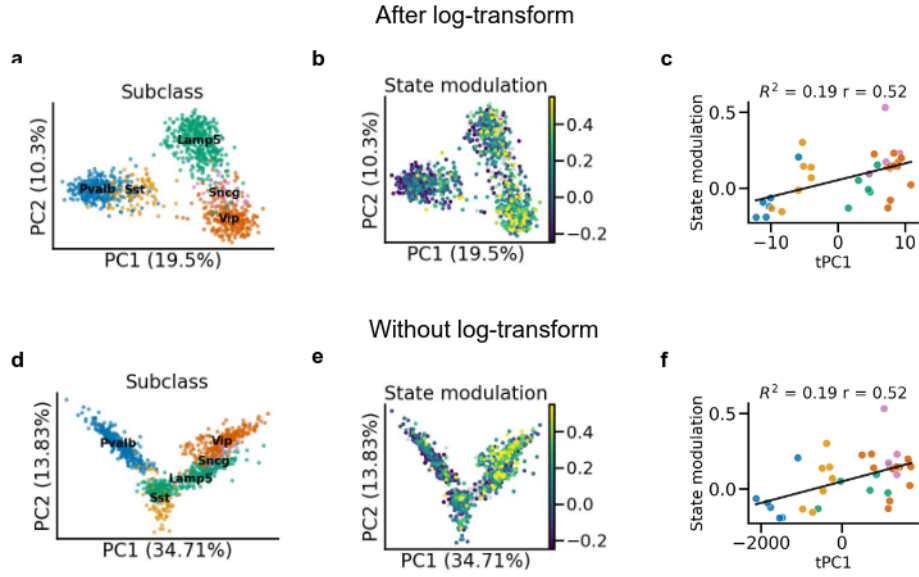
Fig. S3: Log-transformation leads to clustering by developmental origin. (a) First 2 transcriptomic principal components (tPCs) of the log-transformed count RNA data. **(b)** As (a), with colour indicating state modulation. **(c)** The first transcriptomic PC (tPC1) of log-transformed data predicts state modulation, replicated from Fig. S1c for comparison. R^2: leave-one-out fraction of variance explained, r: Pearson correlation. **(d-f)** As (a-c), but without log-transformation. Interneurons now form a continuum along tPC1, but the quantitative relationship between tPC1 and state modulation is preserved (up to 2 digits). Data from Bugeon et al. [9].
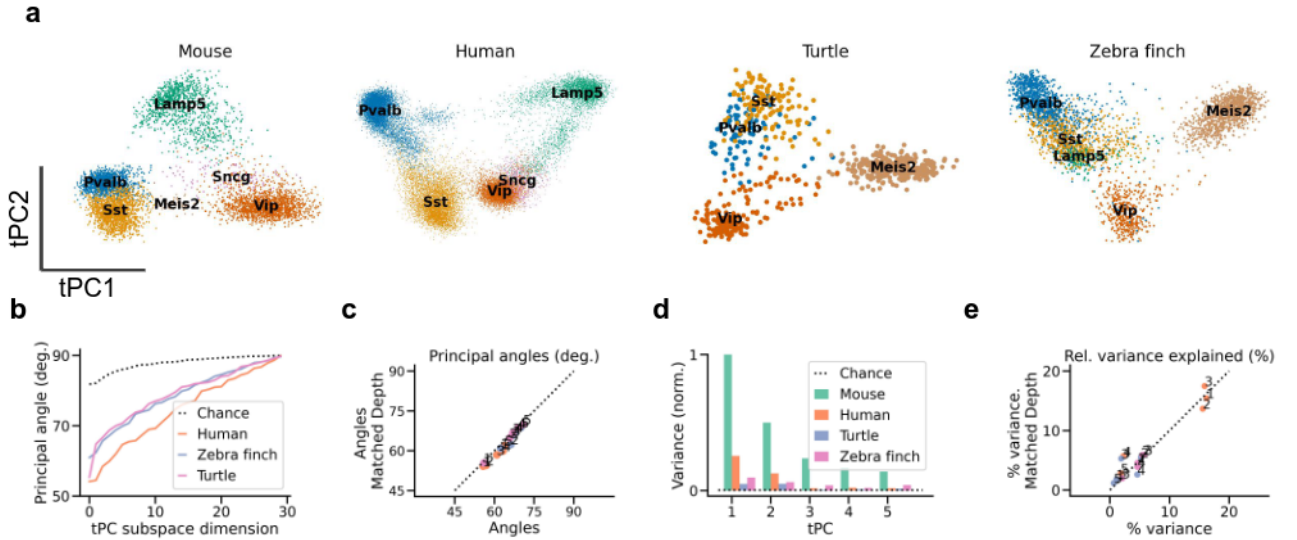
Fig. S4: Transcriptomic PCs robust to sequencing depth. (a) Projection of each dataset onto its first 2 transcriptomic PCs, after subsampling gene counts to the depth of the shallowest dataset (zebra finch, see Table 1). **(b)** Principal angles between tPC subspaces of subsampled data. **(c)** Comparison between angles of full-depth data and subsampled data. **(d,e)** As (b,c) but for variance explained. The human, turtle, and zebra finch tPC1 explain 15.4%, 1.8%, and 4.6% of the variance explained by mouse tPC1, respectively. Data from refs. [6] (mouse), [15] (human), [18] (turtle), [19] (zebra finch).
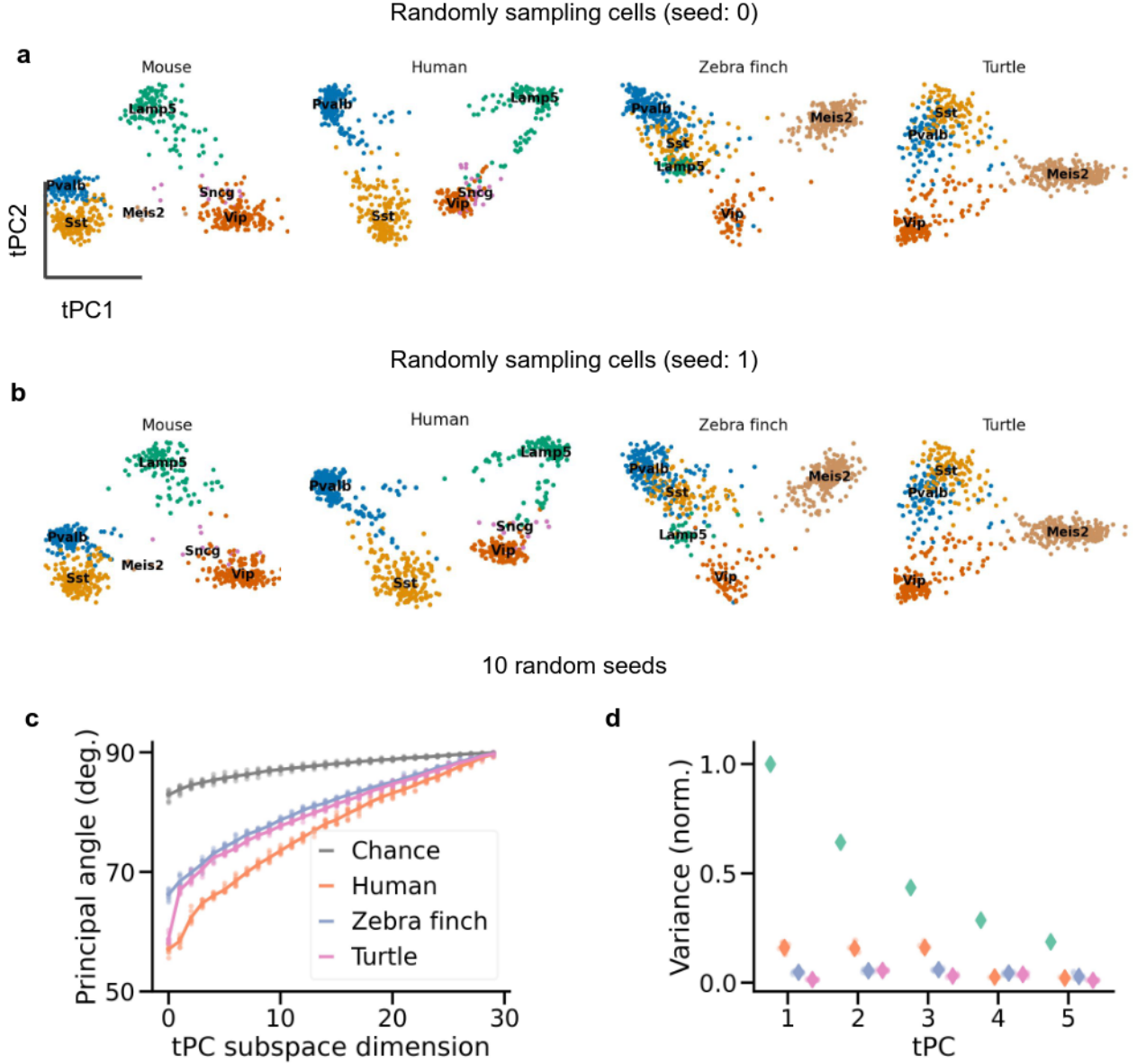
Fig. S5: Differences in tPCs not due to cell count. **(a)** Projection of each dataset onto its first 2 transcriptomic PCs, after random sampling of 640 cells (the number of cells in the smallest dataset, with Turtle cells) without replacement. **(b)** Like (a), but for a different random seed. Note that the Turtle plots in (a) and (b) are the same because there is only one way to sample exhaustively without replacement. **(c)** Principal angles between tPC subspaces. Lines: average across 10 random seeds; dots: individual seeds. **(d)** As (c) but for variance explained, normalized by the variance explained by tPC1 from the mouse data. Diamonds: average across 10 random seeds; dots: individual seeds (largely invisible). Colors as in (c); green dots correspond to the mouse data. Data from refs. [6] (mouse), [15] (human), [18] (turtle), [19] (zebra finch).
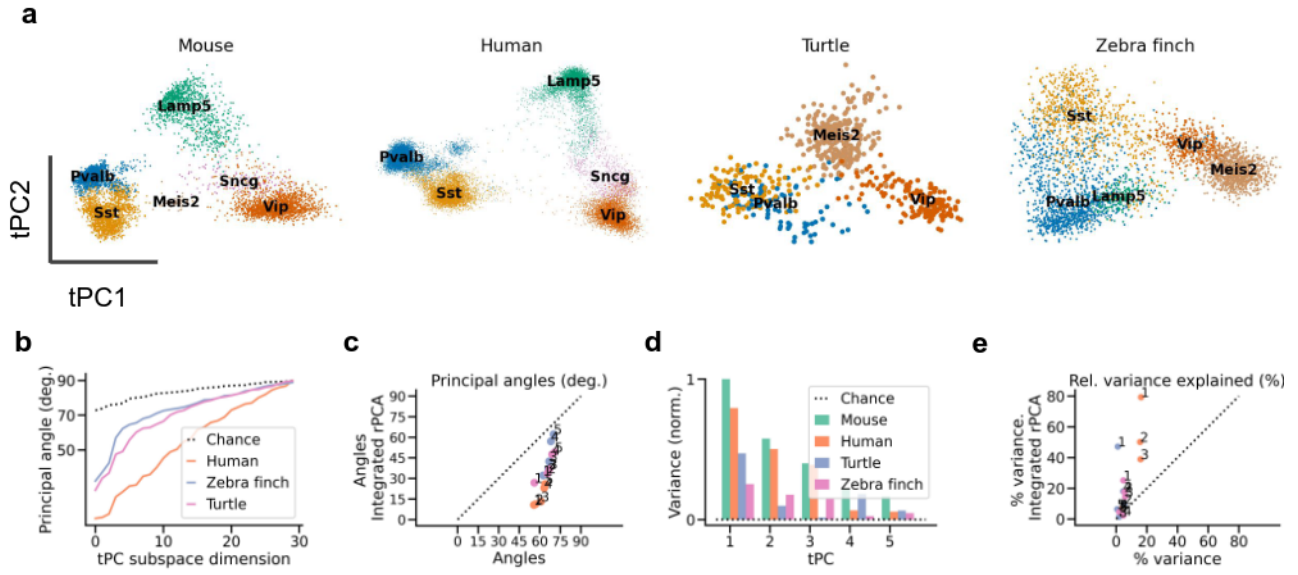
Fig. S6: Computational integration increases similarity of mouse and human data. (a) Projection of each dataset onto its first 2 transcriptomic PCs, after computational integration. Mouse and human datasets show increased similarity, but turtle cells no longer cluster by cell type (colour). **(b)** Principal angles between tPC subspaces computed after integration. **(c)** Comparison between angles computed without integration. Integration increased the similarity of all datasets, especially of the human data. **(d,e)** As (b,c) but for variance explained. The human, turtle, and zebra finch tPC1 explain 79.4%, 47.2%, and 25.2% of the variance explained by mouse tPC1, respectively. Data from refs. [6] (mouse), [15] (human), [18] (turtle), [19] (zebra finch).
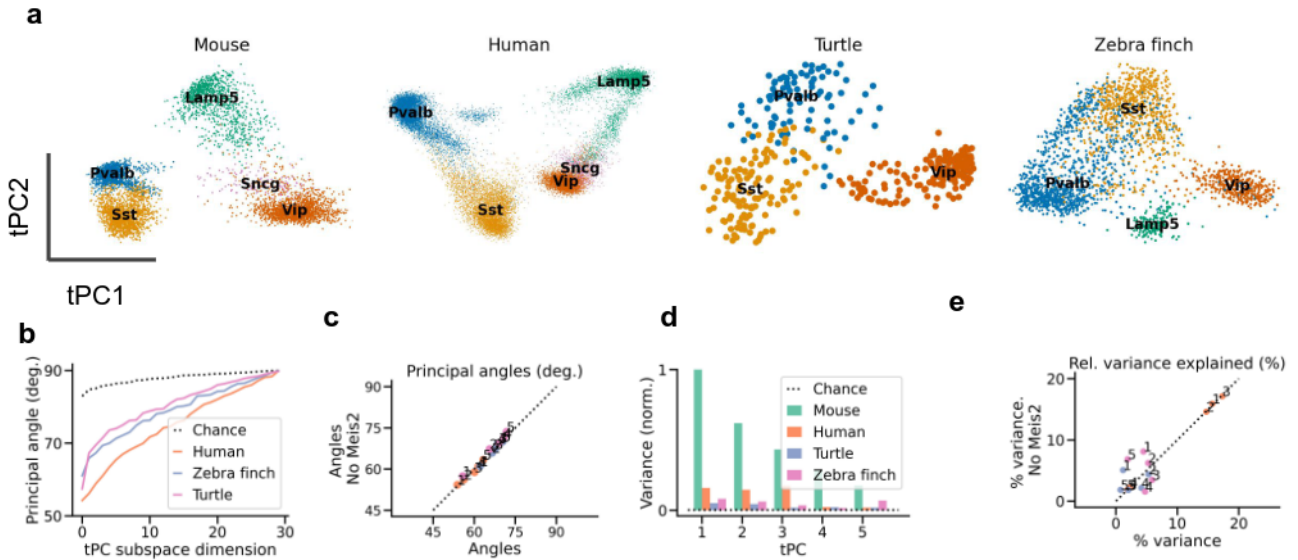

Fig. S7: Differences in tPCs not due to Meis2 cells. (a) Projection of each dataset onto its first 2 transcriptomic PCs, after removing Meis2 cells. **(b)** Principal angles between tPC subspaces computed without Meis2 cells. **(c)** Comparison between angles computed on all cells vs. cells without Meis2 population. **(d,e)** As (b,c) but for variance explained. The human, turtle, and zebra finch tPC1 explain 16.4%, 5.0% and 8.6% of the variance explained by mouse tPC1, respectively. Data from refs. [6] (mouse), [15] (human), [18] (turtle), [19] (zebra finch).
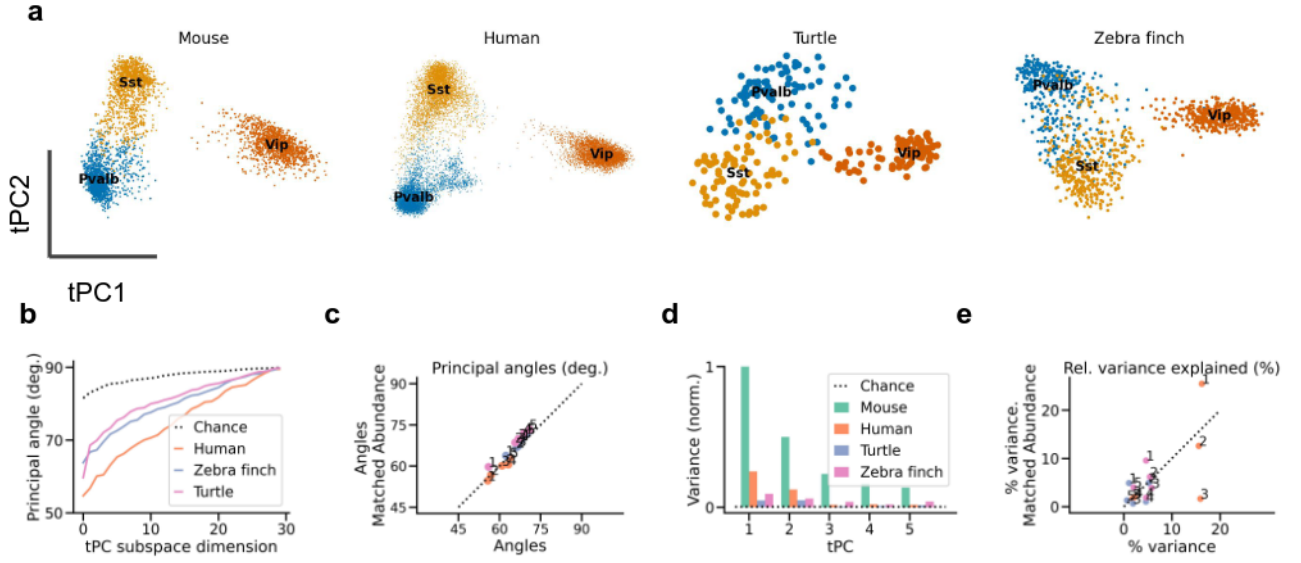
Fig. S8: Differences in tPCs not only due to cell type abundance. (a) Projection of each dataset onto its first 2 transcriptomic PCs, after matching cell type abundances (Fig. 2h). **(b)** Principal angles between tPC subspaces. **(c)** Comparison between angles computed on all cells vs. cells after matching frequencies. **(d,e)** As (b,c) but for variance explained. The human, turtle, and zebra finch tPC1 explain 25.5%, 4.9%, and 9.5% of the variance explained by mouse tPC1, respectively. Data from refs. [6] (mouse), [15] (human), [18] (turtle), [19] (zebra finch).
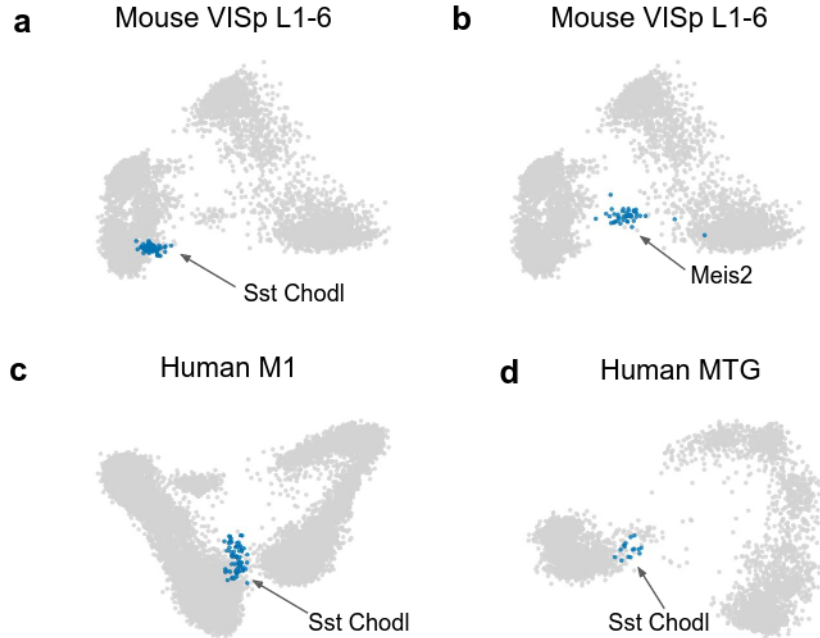

Fig. S9: Intermediate tPC1 position of Chodl and Meis2 neurons. Long range projecting Sst-Chodl **(a)** and white matter Meis2-Adamts19 cells **(b)** occupy an intermedate position along tPC1. **(c,d)** Sst Chodl neurons also have intermediate tPC1 scores in the human data. The human datasets do not contain Meis2 cells. Data from refs. [6] (a,b), [15] (c), and [14] (d).
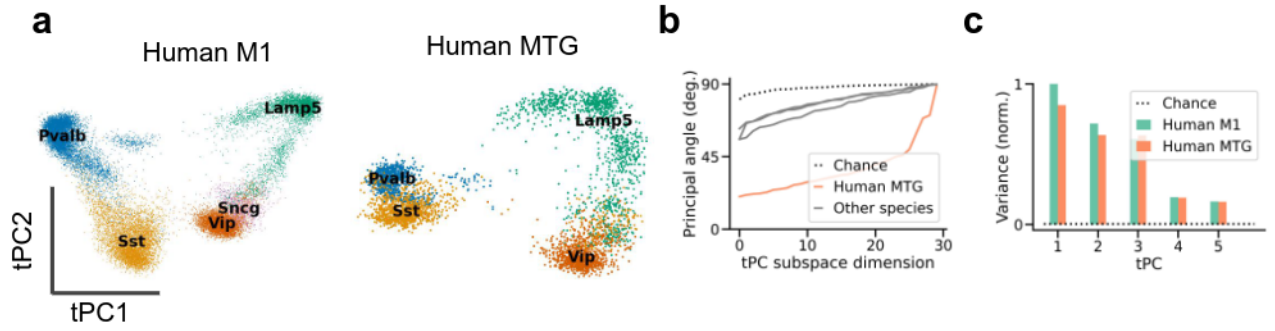
Fig. S10: Small differences in PCs of human datasets. **(a)** Projection of human datasets onto their first 2 tPCs. **(b)** Quantification of tPC similarity using principal angles between tPC subspaces of M1 and MTG data. **(c)** Quantification by variance explained in MTG data. The M1 tPC1 explains 85% of the MTG variance explained by the MTG tPC1. Data from refs. [15] and [14].
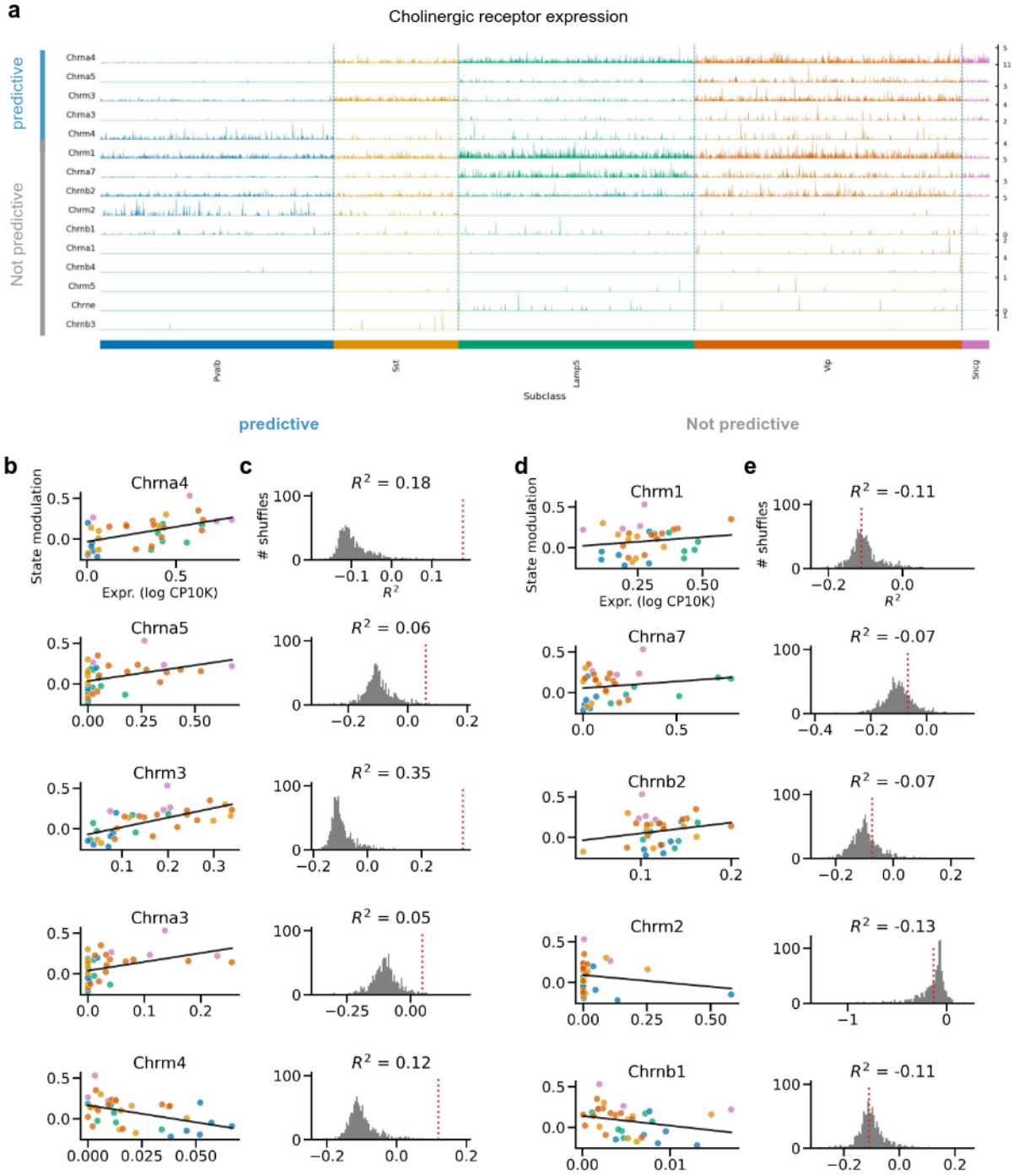
Fig. S11: Predicting state modulation from cholinergic receptor expression. **(a)** Tracks plot of cholinergic receptor (subunit) expression. The first 5 receptors predict state modulation; the remaining 10 do not (see b-e). Predictive and unpredictable receptors are independently sorted by expression based on expression levels. Shown are all receptors with an expression of at least 1 count per 10K. **(b)** Relationship between state modulation and log expression of receptors that are predictive of state modulation (1000 permutations, $p < 0.05$). **(c)** Grey: Null distribution of leave-one-out R^2 estimated by linear regression after permuting expression levels. Red: R^2 without permutation. **(d,e)** As (b,c) but for the 5 unpredictive receptors with the highest expression. Receptor expression from Tasic et al. [6]; state modulation from Bugeon et al. [9].
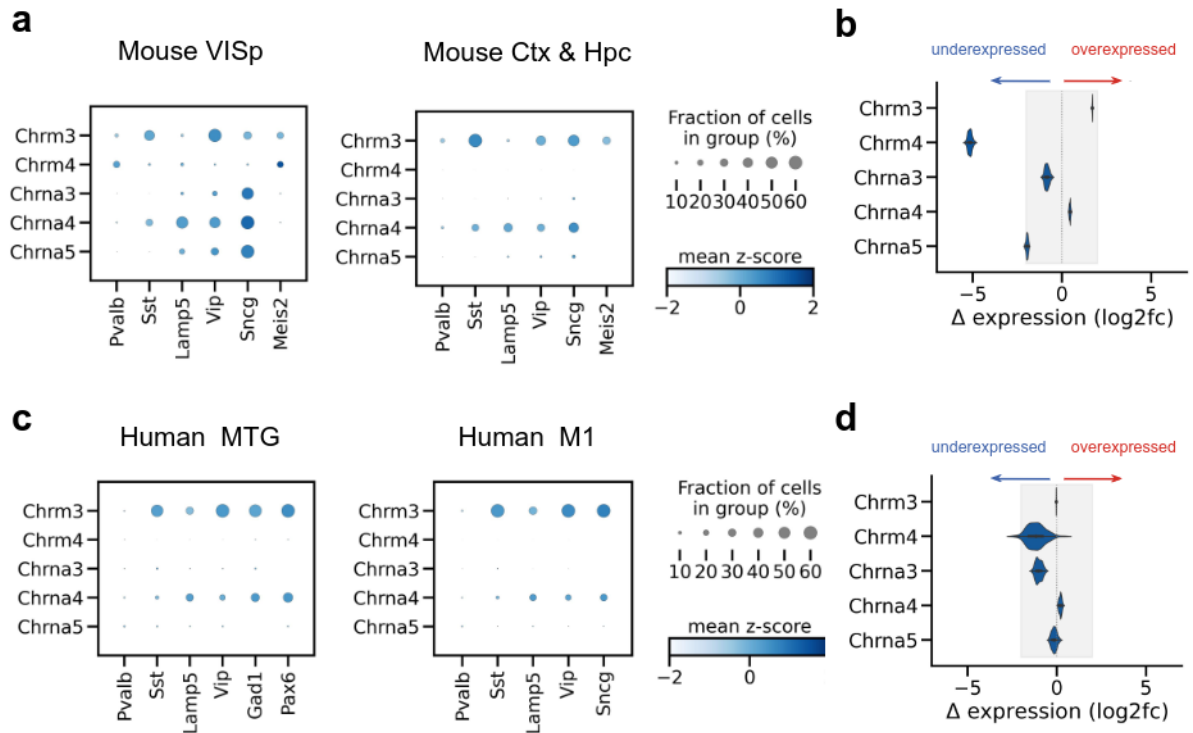
Fig. S12: Mostly small within-species differences in ACh receptor expression. (a) Dot plots showing the expression of the cholinergic receptors that predict state modulation in mouse VISp L1-3 **(b)** Log2-fold differences in expression after downsampling the VISp dataset to equal sequencing depth as the Ctx & Hpc data. Shaded area: log-fold difference of ±2, the range of most within-species differences. The exception is Chrm4, which is underexpressed in the Ctx & Hpc data compared to the VISp data. **(c,d)** As (a,b), but for human datasets. The MTG dataset was downsampled to match the M1 data. Data from refs. [6] (mouse VISp), [29] (mouse Ctx & Hc), [14] (human MTG), and [15] (human M1).